Comparison of Standard and Riemannian Fluid Registration for Tensor-Based Morphometry in HIV/AIDS

Caroline Brun[1], Natasha Lepore[1], Xavier Pennec[2], Yi-Yu Chou[1], Oscar L. Lopez[3], Howard J. Aizenstein[4], James T. Becker[4], Arthur W. Toga[1], and Paul M. Thompson[1]

[1] Laboratory of Neuro Imaging, UCLA, Los Angeles, CA 90095, USA
[2] Asclepios Research Project, INRIA, 06902 Sophia-Antipolis Cedex, France
[3] Department of Psychiatry, University of Pittsburgh, Pittsburgh, PA 15213 USA
[4] Department of Neurology, University of Pittsburgh, Pittsburgh, PA 15213 USA

Abstract. Tensor-based morphometry (TBM) is an analysis approach that can be applied to structural brain MRI scans to detect group differences or changes in brain structure. TBM uses nonlinear image registration to align a set of images to a common template or atlas. Detection sensitivity is crucial for clinical applications such as drug trials, but few studies have examined how the choice of deformation model (regularizer or Bayesian prior) affects sensitivity. Here we tested a new registration algorithm based on a fluid extension of Riemannian Elasticity [17], which penalizes deviations from zero strain in a log-Euclidean tensor framework, but has the desirable property of enforcing one-to-one mappings. We compared it to a standard large-deformation continuum-mechanical registration approach based on hyperelasticity. To compare the sensitivity of the two models, we studied corpus callosum morphology in 26 HIV/AIDS patients and 12 matched healthy controls. We analyzed the spatial gradients of the deformation fields in a multivariate Log-Euclidean framework [1] [12] to map the profile of systematic group differences. In cumulative p-value plots, the Riemannian prior detected disease-related atrophy with greater signal-to-noise than the standard hyperelastic approach. Riemannian priors regularize the full multivariate deformation tensor, yielding statistics on deformations that are unbiased in the associated Log-Euclidean metrics. Compared with standard continuum-mechanical registration, these Riemannian fluid models may more sensitively detect disease effects on the brain.

1 Introduction

Non-rigid image registration has numerous medical applications, including alignment of multi-subject functional and structural images, and multi-modality atlas construction. One increasingly popular application is *tensor-based morphometry*, which registers a set of structural brain images to a common template or atlas, and statistically analyzes the deformations. TBM can detect morphometric differences associated with disease, development or cognitive performance.

Time-dependent changes induced by treatment and disease progression may also be localized and visualized. This method has led to a better understanding of brain growth during normal and abnormal development [21] [6] [10] [18] as well as neurodegenerative diseases such as HIV/AIDS [3] and semantic dementia [20].

Most nonlinear registration algorithms optimize a measure of image similarity between a deforming and a target image, such as the squared intensity differences, cross-correlation or information-theoretic measures such as normalized mutual information or the Jensen-Renyi divergence [3]. A second term, the regularizer, is optimized along with the intensity similarity to enforce desirable properties such as smoothness, invertibility or inverse-consistency [5] [2].

Early registration models used elastic [7] or fluid [4] regularizers, in which registration forces obeyed a continuum-mechanical law. Those forces were applied to the deforming image. Grenander's pattern theory [9] recast these problems in a Bayesian setting, by enforcing statistical prior distributions on the deformations using stochastic PDEs of the form $L\boldsymbol{u} = \boldsymbol{e}$, where L is a self-adjoint 2nd order differential operator, and $\boldsymbol{u}$ and $\boldsymbol{e}$ are the vector-valued displacement field and driving force, respectively. Large deformation diffeomorphic mappings [15] extend this work by constructing energies on velocity fields whose extrema are geodesic paths on groups of diffeomorphisms [23].

Recently, Pennec [16] proposed a deformation prior based on Riemannian elasticity. He defined a corresponding metric using the full deformation tensors $\Sigma = J^T J = (Id + \nabla \boldsymbol{u})^T (Id + \nabla \boldsymbol{u})$, where $\boldsymbol{u}$ is the displacement and J the Jacobian matrix of the transformation, so the approach regularizes all the multivariate information in the tensors. Using the standard Euclidean metric here is not ideal as the deformation tensors Σ live on a conical submanifold of the vector space of matrices with the usual operations. Instead, the log-Euclidean distance is used (see [1]) and incorporated into an hyperelastic registration algorithm. It is based on the distance from these symmetric positive-definite deformation matrices to the identity (the reference point where the deformation is rigid). The resulting method regulates the local anisotropy and orientation changes in a deformation, on top of local expansion factors. The standard Euclidean elastic energy based on the *Saint-Venant Kirchhoff elasticity* is replaced in the Riemannian framework by the log-Euclidean Riemannian elasticity:

$$Reg_{SVKE}(\boldsymbol{u}) = \int \frac{\mu}{4} Tr((\Sigma - Id)^2) + \frac{\lambda}{8} Tr(\Sigma - Id)^2 \tag{1}$$

$$Reg_{LERE}(\boldsymbol{u}) = \frac{1}{4} dist^2_{Eucl}(\log(\Sigma), \log(Id)) = \frac{1}{4} \int ||\log(\Sigma)||^2 \tag{2}$$

which measures differences among tensors accommodating the curvature of the associated manifold of symmetric positive-definite matrices.

Good detection power is crucial for clinical applications, but few studies have examined how the deformation model depending on the regularizer affects disease detection sensitivity in TBM. Most TBM studies create a spatial map of the deformation measures. Statistics are performed on a voxel-by-voxel basis by examining the determinant of J, or more recently, the square root of the

deformation tensors $\sqrt{\Sigma}$ [12]. These depend on the regularizer, but the effects of different regularizers on the sensitivity of the statistics is not well known in real empirical cases. For instance, [11] found that some deformation priors drawn from information theory can remove several sources of statistical bias (e.g., skewness). [12] showed that HIV/AIDS-related atrophy was detected more powerfully by examining multivariate statistics of the deformation tensors in a log-Euclidean space as compared to the commonly used univariate statistics on $detJ$. A statistical prior on the logarithm of the deformation tensors (rather than the scalar logarithm of their determinants) may therefore improve detection power and reduce bias in morphometric studies.

Here, we aim to demonstrate the empirical advantages of the Riemannian elasticity prior proposed in [16] over the standard Euclidean elastic one. The Riemannian prior penalizes deformations directly in the log-Euclidean space of the log-transformed deformation tensors (see [17]), where we later compute our statistics. As a novel contribution, we also extended both of these image registration models to a large-deformation (fluid) approach by applying the priors to the deformation velocity field $\boldsymbol{v}$, i.e. the derivative of $\mathbf{u}$. In [4], it was shown that this achieves large image deformations, while guaranteeing a smooth invertible mapping. To better emphasize the role of the regularizer, we focus on binary images as the information is only located at the edges. The similarity criterion we choose is the sum-of-squared intensity differences, which is reasonable for binary images (we do not consider the intensity cost further in this work, but the formulation here could readily accommodate others as only the body force term would be affected). We compared the results of the Riemannian and Euclidean registrations for the morphometric analysis of 26 HIV/AIDS patients and 12 matched healthy controls. To avoid bias in comparing approaches due to segmentation errors, the corpus callosum of each subject was manually segmented and treated as a binary image that was then nonlinearly registered to one of the controls. We use a single-subject as the target rather than the minimum mean-squared template estimation, as the latter depends on the deformation prior, complicating the interpretation of the results (because the templates would not be the same for different registration methods). To analyze the deformation fields, we used a multivariate statistical method based on the Log-Euclidean metric (see [12]).

2 Methods

2.1 Subjects and Image Acquisition

Twenty-six HIV/AIDS patients (age: 47.2 ± 9.8 yr; 25M/1F; $CD4^+$ T-cell count: $299.5 \pm 175.7/\mu$l; $\log_{10}$ viral load: 2.57 ± 1.28 RNA copies/ml of blood plasma) and twelve HIV-seronegative controls (age: 37.6 ± 12.2 yr; 8M/6F) underwent 3D T1-weighted MRI scanning; the same scans were analyzed in a prior cortical thickness study [22], which also presents the subjects' neuropsychiatric data. All patients met Center for Disease Control criteria for AIDS, stage C and/or 3 and none had HIV-associated dementia. AIDS patients with recent traumatic brain injury, CNS opportunistic infections, lymphoma, or stroke were excluded.

All subjects received 3D spoiled gradient echo (SPGR) anatomical brain MRI scans (256x256x124 matrix, TR = 25 ms, TE = 5ms; 24-cm field of view; 1.5-mm slices, zero gap; flip angle = 40^o) as part of a comprehensive neurobehavioral evaluation. Each subject's brain MRI was co-registered with scaling (9-parameter transformation) to the ICBM53 average brain template, after removing extracerebral tissues (e.g., scalp, meninges, brainstem and cerebellum).

2.2 Elastic versus Fluid Registration

There are two primary classes of methods for registering one image to another. In standard elastic registration (which remains diffeomorphic only for small image deformations), the deformation energy between two images is given by the sum of a similarity measure and a regularization measure that each depend on the displacement $\boldsymbol{u}$. The Navier-Lamé equation was initially used for anatomical image registration. By contrast, fluid registration algorithms regularize the velocity field $\boldsymbol{v}$ rather than the displacement $\boldsymbol{u}$, and this guarantees one-to-one mappings when the velocity field is integrated in time to generate the displacement. [4] [8] considered the deforming image as embedded in a Navier-Poisson fluid:

$$\boldsymbol{F} + \mu\nabla^2\boldsymbol{v}(\boldsymbol{x},t) + (\lambda+\mu)\nabla\nabla^T\boldsymbol{v}(\boldsymbol{x},t) = 0 \tag{3}$$

$\boldsymbol{F}$ is the body force that drives the transformation, μ and λ are viscosity coefficients chosen by the user, and

$$\boldsymbol{v}(\boldsymbol{x},t) = \frac{d\boldsymbol{u}(\boldsymbol{x},t)}{dt} = \frac{\partial\boldsymbol{u}(\boldsymbol{x},t)}{\partial t} + \boldsymbol{v}(\boldsymbol{x},t)\cdot\nabla\boldsymbol{u} \tag{4}$$

Here we use a cost function that minimizes the squared intensity difference between the two images. Its gradient yields the body force:

$$\boldsymbol{F}(\boldsymbol{x},\boldsymbol{u}(\boldsymbol{x},t)) = -[T(\boldsymbol{x}-\boldsymbol{u}(\boldsymbol{x},t)) - S(\boldsymbol{x})]\nabla T|_{\boldsymbol{x}-\boldsymbol{u}(\boldsymbol{x},t)} \tag{5}$$

2.3 Regularizer

Instead of the Navier-Poisson fluid formulation, here we directly regularize the deformation tensors, as they are ultimately the measures that are analyzed in TBM. We build on [17], where a regularizer is defined in a Riemannian framework on the Σ's to quantify the amount of deformation. This penalty (2) can be made more complex either by considering the anisotropic (non-homogeneous) case or by requiring that the norm be globally inverse-consistent. Here, we do not consider these variants, and evaluate the new regularizer in the isotropic case. Using $||\Sigma||^2 = Tr(\Sigma^2)$, the formula for the regularizer takes the simple form

$$Reg_{ILERE}(\boldsymbol{u}) = \int \frac{\mu}{4}Tr((\log(\Sigma)^2) + \frac{\lambda}{8}Tr(\log(\Sigma))^2 \tag{6}$$

In the fluid case, we regularize $\boldsymbol{v}$ rather than $\boldsymbol{u}$ during the registration. Thus we implemented the term $\log((\nabla \boldsymbol{v} + Id)^T(\nabla \boldsymbol{v} + Id))$ instead of $\log(\Sigma)$ in our fluid registration algorithm. Eq. (6) becomes

$$\begin{aligned} Reg_{Riem}(\boldsymbol{v}, t) = \int \tfrac{\mu}{4} Tr(\log((\nabla \boldsymbol{v} + Id)^T(\nabla \boldsymbol{v} + Id))^2) \\ + \tfrac{\lambda}{8} Tr(\log((\nabla \boldsymbol{v} + Id)^T(\nabla \boldsymbol{v} + Id)))^2 \end{aligned} \tag{7}$$

Thus, our final fluid equation is

$$\frac{d\boldsymbol{v}(\boldsymbol{x}, t)}{dt} = \boldsymbol{F} + \nabla Reg(\boldsymbol{v}, t) \tag{8}$$

Here Reg is $Reg_{Riem}(\boldsymbol{v}, t)$ or the standard Euclidean hyperelastic regularizer $Reg_{Eucl}(\boldsymbol{v}, t) = \int \frac{\mu}{4} Tr((\nabla \boldsymbol{v} + Id)^2) + \frac{\lambda}{8} Tr(\nabla \boldsymbol{v} + Id)^2$.

2.4 Numerical Solution

Registration aims to find a displacement field mapping the study onto the template. As our regularizing functionals contain nonlinear terms depending on both $\boldsymbol{u}$ and $\boldsymbol{v}$, computing $\boldsymbol{u}$ is not straightforward. First, a multiresolution algorithm is used to solve the Partial Differential Equation (PDE). The computed velocity field is considered as a Lagrangian velocity given that the time steps are infinitesimal. At each time t, a force is calculated depending upon the previous displacement. The velocity is then found using a gradient-descent method based on *Levenberg-Marquardt* optimization, and integrated to find the displacement. This approach is termed a 'greedy' algorithm; other regularizers could be used instead that generate geodesics on the space of diffeomorphisms by defining energies on the full space-time path of the deformation. A supplementary step is needed to prevent singularities. If the Jacobian falls below a threshold (here 0.5), a regriding step is performed [4]. The algorithm is as follow:

1. Define a grid on the template and an initial resolution; initialize $t = 0$ and $\boldsymbol{u}(\boldsymbol{x}, t = 0) = \boldsymbol{0}$
2. Calculate the force, i.e. the gradient of the mean square difference eqn. 5 at this given resolution.
3. Solve the PDE to find the velocity at the same resolution, at each point in the grid, using gradient descent. We chose $\boldsymbol{v}_0 = \eta G \circ \boldsymbol{F}$ with $\eta = 0.1$ and G is a Gaussian function. $\boldsymbol{v_{n+1}} = \boldsymbol{v_n} - \epsilon(\boldsymbol{v_n} - \boldsymbol{F} + \alpha \nabla Reg_{Riem})$ (α is the weight given to the regularizer)
4. Find a time step that is consistent with the maximal flow allowed in deformation.
5. Integrate $\boldsymbol{v}$ to find $\boldsymbol{u}$, with this time step.
6. Compute the Jacobian of the displacements. If the Jacobian determinant falls below 0.5, then re-grid the template and return to Step 4.
7. Obtain the new displacement field once the Jacobian value is acceptable.

3 Results

Figures 1 a. and b. show different registrations with O- and C- shaped geometries and gray scale phantoms. Boundaries are accurately matched by both registration methods even when large deformations and gray scale modification are required. Fig 1c. shows thresholded statistical maps of local differences in the corpus callosum between the HIV/AIDS group and controls. These are based on multivariate (Hotelling's T-squared) statistics on the full deformation tensors, which incorporate information on local orientations, directional scaling and areal differences. Green colors show regions for which $p < 0.05$ locally. The Riemannian prior arguably outperforms the Euclidean one as it can detect significant differences that are undetected with the Euclidean prior. This makes sense as the Riemannian prior regularizes the tensor-valued quantity used to compute the statistics. To emphasize the difference between the distributions, in each case we plotted the cumulative distribution function of the p-values against the corresponding p-value that would be expected under the null hypothesis (of no group difference). For a null distribution, this plot falls along the line $x = y$, as represented by the dotted line. Steeper upward inflections of this curve are associated with significant signal and greater effect sizes (Fig 1.c.) (see [14]). This CDF approach has been used in [13] to compare effect sizes in TBM, and is based on the False Discovery Rate concept used in imaging statistics for multiple comparison correction [19].

4 Discussion

Using two different registration methods to warp the images, and the same multivariate statistical analysis, we showed that the deformation model (regularizer) greatly influences the sensitivity for detecting anatomical findings in TBM. In HIV/AIDS, previous studies using parametric mesh methods showed an anatomically distributed profile of differential atrophy (reduced thickness) in the corpus callosum [22]. The Riemannian fluid prior confirmed these results, while the Euclidean hyperelastic prior showed a subtle and more anatomically restricted alteration in the corpus callosum. Although the prior obviously has an impact on the statistical analysis, this study is one of surprisingly few TBM studies that have examined its effect. There are two caveats regarding our analysis. First, the extent of atrophy in HIV is strictly speaking unknown, although pathological studies support the notion of regional atrophy. Future studies will aim to find the optimal prior in a predictive statistical design (e.g. predicting future clinical deterioration), where ground truth is known, and the relative power of any detected signal can be independently established. Second, our current disease sample could not be matched precisely for age or sex with the controls, who were slightly younger on average, so we cannot rule out that age effects might contribute to the effects mapped here. Future studies will address the etiology of the signals, but it is clear now that different priors detect tensor differences with different levels of power, motivating future empirically-driven and theoretical work on priors in deformation morphometry.

References

1. Arsigny V. et al., *Log-Euclidean metrics for fast and simple calculus on diffusion tensors*, Mag Res Med 56, (2006) 411-421
2. Cachier P. et al., *Symmetrization of the Non-Rigid Registration Problem using Inversion-Invariant Energies: Application to Multiple Sclerosis*, MICCAI, Pittsburgh, PA, USA, (2000) 472-481
3. Chiang MC et al., *3D pattern of brain atrophy in HIV/AIDS visualized using tensor-based morphometry*, Neuroimage (2007)
4. Christensen GE et al., *Deformable templates using large deformation kinematics*, IEEE Trans. Image Process. 5, (1996) 1435-1447
5. Christensen GE et al., *Consistent Image Registration*, IEEE TMI 20, (2001) 568-582
6. Chung MK et al., *A Unified Statistical Approach to Deformation-Based Morphometry*, Neuroimage, 14, (2006) 595-606
7. Davatzikos C. et al., *A computerized approach for morphological analysis of the corpus callosum*, JCAT 20, (1996) 88-97
8. Gramkow C., *Registration of 2D and 3D medical images*, Master's thesis, Danish Technical University, Copenhagen, Denmark (1996)
9. Grenander U. et al, *Computational anatomy: An emerging discipline*, Quart. of App. Maths 56, (1998) 617-694
10. Lee AD et al., *3D Pattern of Brain Abnormalities in Fragile X Syndrome Visualized using Tensor-Based Morphometry*, Neuroimage, (2006)
11. Leow AD et al., *Statistical properties of Jacobian maps and inverse-consistent deformations in non-linear image registration* IEEE TMI 26, (2007) 822-832
12. Lepore N. et al., *Multivariate Statistics of the Jacobian Matrices in Tensor-Based Morphometry and their application to HIV/AIDS*, MICCAI, Copenhagen, Denmark (2006)
13. Lepore N. et al., *Mean template for Tensor-Based Morphometry using deformation tensors*, MICCAI, Brisbane, Australia (2007)
14. Manly K. et al., *Genomics, Prior Probability, and Statistical Tests of Multiple Hypotheses*, Genome Research 14, (2004) 997-1001
15. Miller MI, *Computational anatomy: shape, growth and atrophy comparison via diffeomorphisms*, Neuroimage 23, (2004) 19-33
16. Pennec X. et al., *Riemannian elasticity: A statistical regularization framework for non-linear registration*, MICCAI, Palm Springs, CA, USA, (2005) 943-950
17. Pennec X., *Left-invariant Riemannian elasticity: a distance on shape diffeomorphisms?*, MFCA, Copenhagen, Denmark, (2006) 1-13
18. Rueckert D. et al., *Diffeomorphic Registration using B-Splines*, MICCAI, Copenhagen, Denmark (2006)
19. Storey JD, *A Direct Approach to False Discovery Rates*, J.R. Stat. Soc. B 64, (2002) 479-498
20. Studholme C. et al., *Deformation tensor morphometry of semantic dementia with quantitative validation*, Neuroimage 21, (2004) 1387-1398
21. Thompson PM et al., *Growth Patterns in the Developing Brain Detected By Using Continuum-Mechanical Tensor Maps*, Nature 404, (2000) 190-193
22. Thompson PM et al., *Thinning of the cerebral cortex visualized in HIV/AIDS reflects CD4+ T-lymphocyte decline*, PNAS 102, (2005) 15647-15652
23. Wang L et al., *Large deformation diffeomorphism and momentum based hippocampal shape discrimination in dementia of the Alzheimer type*, IEEE TMI 26, (2007) 462-470

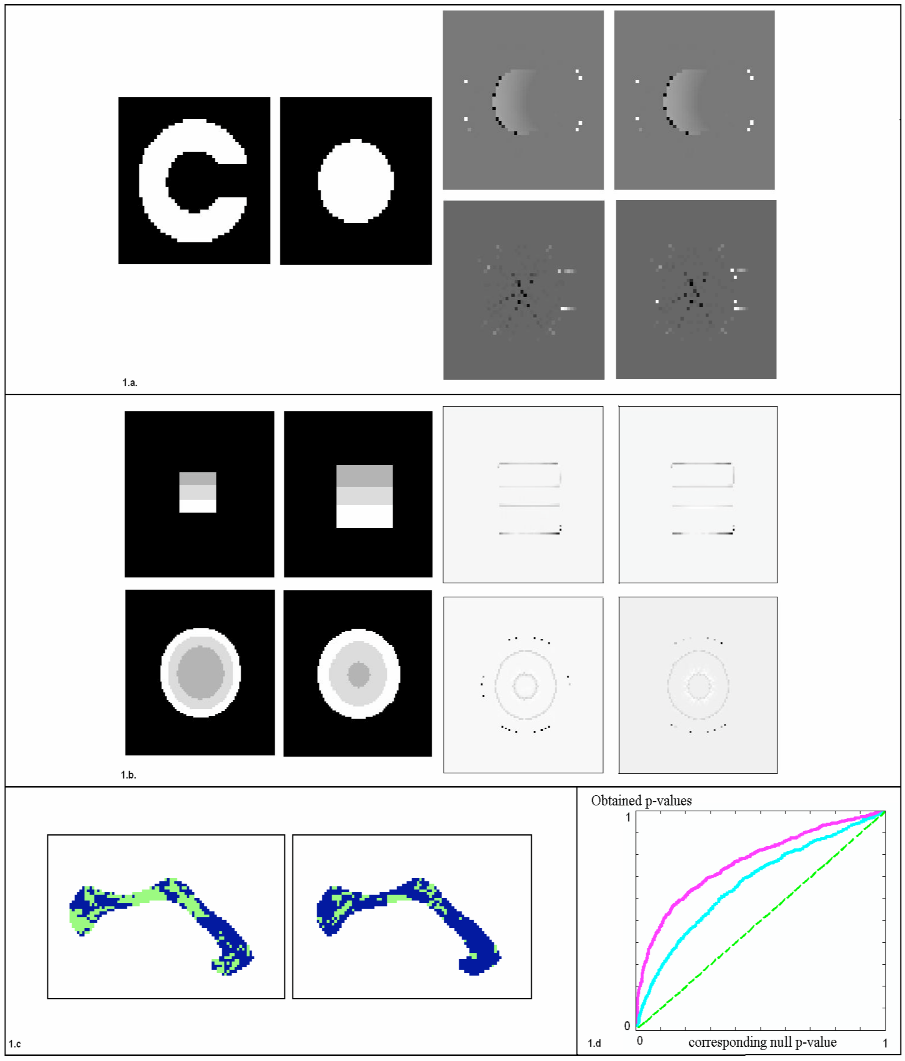

Fig. 1. Top left: C-shaped and O-shaped phantoms (left); difference between the target and the deformed template after fluid registration based on the Riemannian (left) and Euclidean prior (right) (fixed image: C, moving image: O (top) and *vice versa* (right) **Top right:** gray scale phantoms (deforming image (left) fixed target image (right)) difference between the template and the registered image using the fluid registration based on the Riemannian (left) and Euclidean prior (right). Here, $\mu = 1.5$ and $\lambda = 0.5$ **Bottom left:** p-values obtained after registration with the two different priors. Green regions show morphometric differences where $p < 0.05$. Left: map based on registration with the Riemannian prior Right: map based on registration with the Euclidean prior **Bottom right:** Cumulative distribution functions of observed p-values vs the corresponding null p-value for each of the multivariate statistics: Euclidean prior (cyan), Riemannian prior (magenta). The dotted line shows the expected distribution of p-values under the null hypothesis.